Chemical Science

ROYAL SOCIETY OF CHEMISTRY

EDGE ARTICLE

View Article Online
View Journal | View Issue

Cite this: *Chem. Sci.*, 2023, **14**, 4091

All publication charges for this article have been paid for by the Royal Society of Chemistry

Bent-to-planar Si-rhodamines: a distinct rehybridization lights up NIR-II fluorescence for tracking nitric oxide in the Alzheimer's disease brain†

Qingshuang Xu,‡[a] Yutao Zhang,‡[a] Mingming Zhu,[b] Chenxu Yan,[a] Wenle Mao,[a] Wei-Hong Zhu[a] and Zhiqian Guo*[a]

An ongoing revolution in fluorescence-based technologies has transformed the way we visualize and manipulate biological events. An enduring goal in this field is to explore high-performance fluorogenic scaffolds that show tunability and capability for *in vivo* analysis, especially for small-molecular near-infrared (NIR) fluorophores. We present a unique bent-to-planar rehybridization design strategy for NIR fluorogenic scaffolds, thus yielding a palette of switchable bent/planar Si-rhodamines that span from visible to NIR-II wavelengths. We demonstrate that the rehybridization of *meso*-nitrogen in this innovative NIR scaffold Cl-SiRhd results in flipping between the disruption and recovery of the polymethine π-electron system, thereby significantly altering the spectral wavelength with crosstalk-free responses. Using elaborately lighting-up NIR-II probes with ultra-large Stokes shifts (*ca.* 250 nm), we successfully achieve real-time *in situ* monitoring of biological events in live cells, zebrafish, and mice. Notably, for the first time, the light-up NIR-II probe makes a breakthrough in directly *in situ* tracking nitric oxide (NO) fluctuations in the brains of mice with Alzheimer's disease. This *de novo* bent-to-planar rehybridization strategy of NIR-II probes opens up exciting opportunities for expanding the *in vivo* imaging toolbox in both life science research and clinical applications.

Received 12th January 2023
Accepted 4th March 2023

DOI: 10.1039/d3sc00193h

rsc.li/chemical-science

Introduction

Fluorescence-based technologies have changed the way we study life science and conduct diagnostics.[1–5] Most prominent amongst these enabling technologies is the utility of fluorescent probes for *in vivo* tracking of biological events with high resolution.[6–9] Probes with near-infrared (NIR) emission are extremely important, but the primary hurdle is the lack of novel NIR-II fluorogenic scaffolds, showing powerful tunability and capability for *in vivo* analysis. Most efforts rely on conjugated π-expansion and donor–acceptor (D–A) adjustment (Fig. 1A).[10–12] However, most of the current NIR-II fluorophores usually require difficult and laborious synthesis and inflict self-instability along with undesirable quenching.[12–16] Nowadays, it is urgent to develop an innovative NIR-II fluorogenic framework for highly accurate *in vivo* sensing and clinical translation.

Various fluorophores, including Si-rhodamines, have been widely used across a variety of fields including chemistry and life sciences.[17–20] For instance, the element-substitution strategy that replaces the oxygen-bridge atom with a silicon atom in the xanthene core could alter the energy level of both HOMO and LUMO simultaneously, thereby narrowing the bandgap to afford considerable spectral red-shifts.[21] Notably, Si-rhodamines afford a longer wavelength, superior brightness, and photostability, making them an outstanding candidate for *in vivo* bioimaging.[22,23] However, this merely element-substitution skeleton modification alone limits the emission window expanding into the NIR-II window. Inspired by π-extension from molecular conformation changes, we hypothesize that one reasonable solution for developing an innovative NIR-II fluorogenic platform could be attained by tailoring the conjugated skeleton and switchable delocalization, that is greatly expanding the spectral windows and lighting up NIR fluorescence intensity.

[a]*Key Laboratory for Advanced Materials and Joint International Research Laboratory of Precision Chemistry and Molecular Engineering, Shanghai Key Laboratory of Functional Materials Chemistry, Shanghai Frontier Science Research Base of Optogenetic Techniques for Cell Metabolism, Frontiers Science Center for Materiobiology and Dynamic Chemistry, Institute of Fine Chemicals, School of Chemistry and Molecular Engineering, East China University of Science & Technology, Shanghai 200237, China. E-mail: guozq@ecust.edu.cn*

[b]*Division of Gastroenterology and Hepatology, Key Laboratory of Gastroenterology and Hepatology, Ministry of Health, Inflammatory Bowel Disease Research Center, Renji Hospital, School of Medicine, Shanghai Institute of Digestive Disease, Shanghai Jiao Tong University, Shanghai, China*

† Electronic supplementary information (ESI) available: Additional experimental details and data. CCDC 2119838, 2119842 and 2132279. For ESI and crystallographic data in CIF or other electronic format see DOI: https://doi.org/10.1039/d3sc00193h

‡ Q. X. and Y. Z. contributed equally to this work.

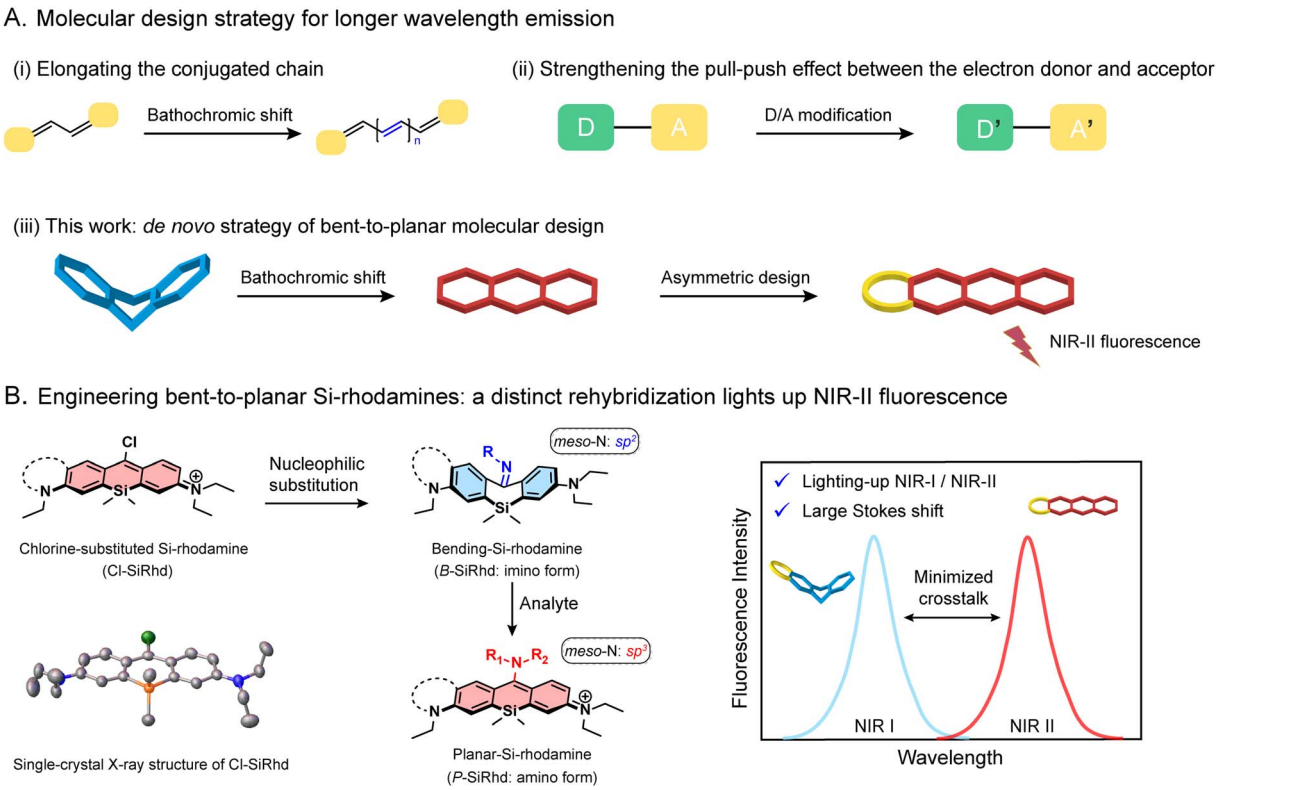

Fig. 1 *De novo* concise design strategy of bent-to-planar fluorophores enables switchable NIR-II emission. (A) Schematic illustration of structural engineering for NIR-I/NIR-II emission fluorophores: (i) elongating the conjugated chain, (ii) strengthening the pull–push effect between the electron donor and acceptor, (iii) in our strategy, molecular bent-to-planar configuration-switches exploring a distinct gateway to NIR-II emission. (B) The change in the hybridization state of *meso*-nitrogen in the Cl-SiRhd scaffold can switch intramolecular π-electron delocalization and therefore result in flipping between the disruption and recovery of the polymethine π-electron system: imino form with a bent configuration, and amino form with a planar configuration, respectively.

Herein, we report a *de novo* design strategy to construct bent-to-planar NIR-II fluorophores based on a discovered fluorogenic platform, *i.e.*, *meso*-chlorine substituted Si-rhodamine (Cl-SiRhd, Fig. 1B). Through the nucleophilic substitution at the *meso*-position, π-conjugation of these Si-rhodamines becomes switchable, thereby initiating a new method of analyte controlled molecular configuration changes. We expand this bent-to-planar molecular strategy on this novel Cl-SiRhd scaffold to engineer a series of Si-rhodamine probes spanning from the visible to NIR-II range. We demonstrate that the change in the hybridization state of *meso*-nitrogen in this Cl-SiRhd scaffold could result in flipping between the disruption and recovery of the polymethine π-electron system, thereby significantly altering the spectral wavelength. Specifically, the imino forms of sp^2-hybridized *meso*-nitrogen generate a bent configuration and short wavelengths; the corresponding amino forms cause planar configuration with long wavelengths (Fig. 1B). Using these switchable bent/planar Si-rhodamines, we have constructed various crosstalk-free ratiometric probes, especially for highly favorable turn-on NIR-II probes with large Stokes shifts (*ca.* 250 nm). Notably, these configuration-dependent Si-rhodamine probes allow us to noninvasively and real-time monitor biological events in live cells, zebrafish, and mice. For the first time, the elaborately lighting-up NIR-II Si-rhodamine probes make a breakthrough in directly tracking nitric oxide (NO) fluctuation in the Alzheimer's disease (AD) brain of mice. This accessible bent-to-planar strategy opens up further exciting opportunities for developing NIR-II probes, facilitating the advancement of highly accurate analysis *in vivo*.

Results and discussion

Engineering *meso*-chlorine substituted Si-rhodamine chromophores

Aiming to expand the utility of fluorophores along with tailoring their emission properties for *in vivo* bioimaging, many research studies were devoted to Si-rhodamines.[24–26] We noted that the modification of *meso*-substituents in xanthene and cyanine skeletons could afford significant spectral changes.[27–31] For instance, amination or hydroxylation on *meso*-chloride cyanine dyes could significantly disturb the conjugated system.[32,33] Here, we firstly discovered and obtained chemically reactive *meso*-chlorine substituted Si-rhodamines, *i.e.*, Cl-SiRhd (Fig. 1B), which allows various *meso*-substitutions under mild conditions, thus regulating the nature of the conjugated system. Similar to Cl-cyanine, Cl-SiRhd can be substituted with nucleophiles to produce a variety of NIR fluorophores and probes, and due to the superior stability and quantum efficiency of Si-

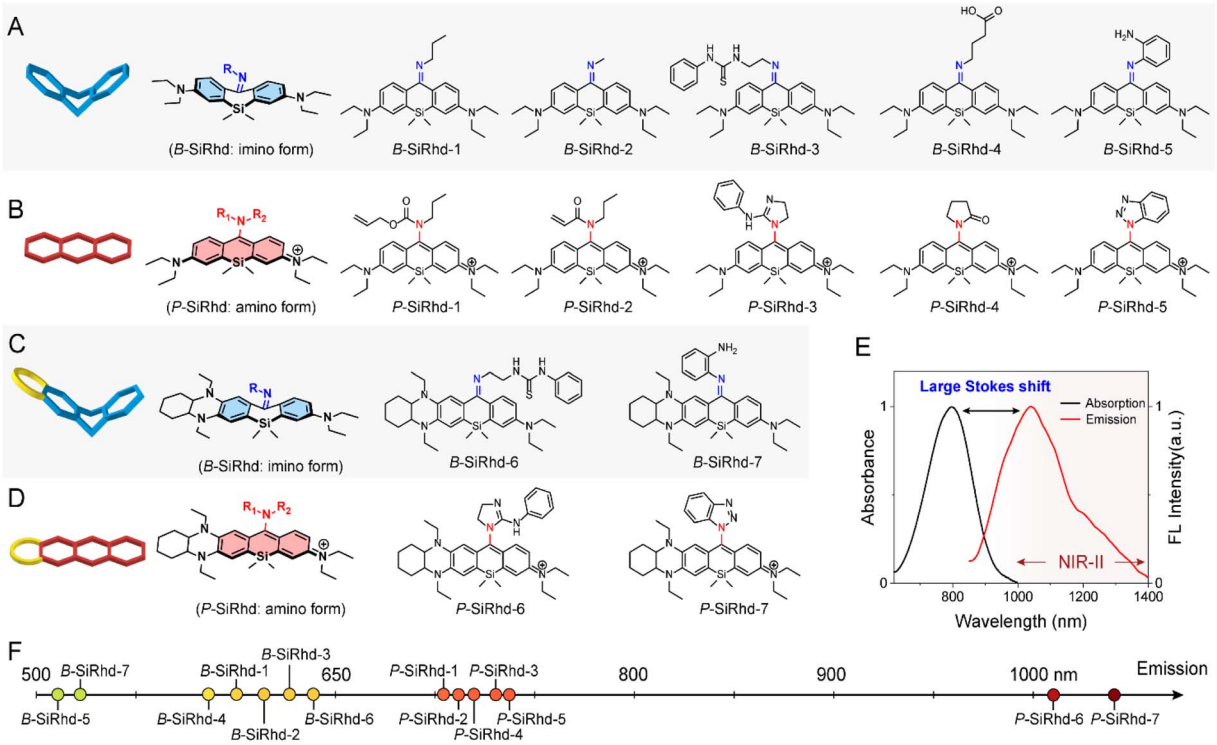

Fig. 2 Regulation π-electron delocalization induced spectral shift in Si-rhodamine fluorophores. Chemical structures of (A and C) bent-Si-rhodamine (B-SiRhd) and (B and D) planar-Si-rhodamine (P-SiRhd) fluorophores. (E) Normalized absorption and fluorescence spectra of representative asymmetric P-SiRhd-7 with a large Stokes shift. (F) Emission maxima peaks of bent/planar Si-rhodamines are visualized graphically on the electromagnetic spectrum.

rhodamine dyes, we expect that Cl-SiRhd has great potential for the development of *in vivo* fluorescent diagnostic reagents. To gain further insight into the structure–property relationship of the spectral changes, *via* nucleophilic amination, a series of *meso*-nitrogen substituted Si-rhodamines were portable synthesized (Fig. 2).

As is well-known, it's extremely difficult to regulate the emission spectra in a "given" Si-rhodamine scaffold with a large Stokes shift.[23,26,34] However, our obtained Si-rhodamine probes show unprecedented and distinct spectral changes: (i) the resulting imino form of Si-rhodamines (such as B-SiRhd-1; λ_{em} = 600 nm) showed short-wavelength emission (Fig. 2F and S1–S3†); (ii) when *meso*-nitrogen becomes more electron poor, the corresponded amination of Si-rhodamines (such as P-SiRhd-1; λ_{em} = 700 nm) displayed long-wavelength emission (Fig. 2F and S4–S7†). Thus, these changes of the *meso*-nitrogen substituent in the conjugation play a key role in both absorption and emission spectral changes. As mentioned above, the hybridized nature of the *meso*-nitrogen substituent in this Cl-SiRhd scaffold responsible for the significant spectral shift is highly unusual in a "given" Si-rhodamine scaffold and needs to be further investigated.

Starting from the initial B-SiRhd-1 and P-SiRhd-1, we engineered a series of wavelength-regulable Si-rhodamines using the following guidelines (Fig. 1B): (i) starting with Cl-SiRhd as the fluorogenic motif; (ii) regulating *meso*-nitrogen with nucleophilic substituents. This strategy unlocks a great opportunity to rapidly establish a library of Si-rhodamines for studying the regularity of their spectra. Specifically, we employed propylamine, 1-(2-aminoethyl)-3-phenylthiourea, and 4-aminobutyric acid, thus forming imine-type structures; while allyl propylcarbamate, guanidine derivatives, and pyrrolidinone as amine-type structures (Fig. 2). To our delight, all the resulting imino forms of Si-rhodamines displayed relative short-wavelength emission (Fig. S8†), whereas their corresponding amino forms of Si-rhodamines exhibited much longer emission (Fig. S9†). More importantly, when we elaborately constructed an asymmetric Si-rhodamine fluorogenic scaffold, the resulting Si-rhodamines (P-SiRhd-6 and P-SiRhd-7) achieved unexpected maximum NIR-II emission around 1050 nm (Fig. 2E, F and S10†). As far as we know, for the first time, a simple and generalizable Si-rhodamine engineering strategy was formulated to induce large spectral shifts spanning from the visible to NIR-II range (emission from 520 nm to over 1050 nm).

Revealing the bent-to-planar configuration changes

To get a deeper understanding of these significant spectral shifts, it's critical to obtain the molecular geometries/configuration of these Si-rhodamines. It has been revealed that modifying the amino group at the *meso*-position of the xanthene scaffold could significantly alter the spectral properties of Si-rhodamines.[35–37] Fortunately, we acquired single crystals of B-SiRhd-5 and P-SiRhd-2 (Fig. 3A and B). Specifically, B-SiRhd-5 possesses a large dihedral angle (around 37.15°)

between two benzene units (Fig. 3A). With the attachment of the amino-group with an acryloyl unit, the resulting P-SiRhd-2 exhibits an almost coplanar configuration (Fig. 3B, with merely a 5.76° dihedral angle between two benzene groups). According to single-crystal analysis, the dihedral angle between two benzene rings is distinctly different from the electron density perturbation of *meso*-nitrogen substituents. These results elucidated that the regulation of the *meso*-nitrogen substitution of these B-SiRhd/P-SiRhd chromophores plays a key role in their molecular configuration. Thus, we reasoned that B-SiRhd-5 has a bent configuration with a shorter emission due to its obviously disrupted π-conjugation system. In contrast, P-SiRhd-2 with much longer emission exhibits planar configuration, maintaining the "unbroken" polymethine π-delocalization.

Subsequently, we investigated the role of *meso*-substituent in switching the intramolecular π-electron delocalization. Two (or more) consecutive carbon–carbon single bonds generally disrupt the π-electron delocalization in a conjugated system. Indeed, the bent B-SiRhd-5 (imino form) possesses an obvious double bond (1.29 Å) of the C=N bond between *meso*-nitrogen and central-carbon C_5, and therefore this sp^2 hybridization of the N atom leads to two consecutive single bonds C_4–C_5 and C_5–C_6 in this Si-rhodamine (Fig. 3A and C). In contrast, the planar P-SiRhd-2 (amino form) exhibits a single bond (1.45 Å) of the C–N bond between *meso*-nitrogen (sp^3 hybridization) and central-carbon atoms. Importantly, in P-SiRhd-2, no consecutive single carbon bonds are found in its skeleton (Fig. 3B and D), thereby affording much longer emission than that of B-SiRhd-5. Collectively, these results elucidate that the hybridization of *meso*-nitrogen in these B-SiRhd/P-SiRhd skeletons could switch the π-electron delocalization: (i) C=N bond formation disrupts π-electron delocalization with a bent fluorophore scaffold (Fig. 3A and C); (ii) *meso*-nitrogen undergoing sp^3-hybridization restores π-electron delocalization with a planar fluorophore scaffold (Fig. 3B and D). Given that changing the molecular

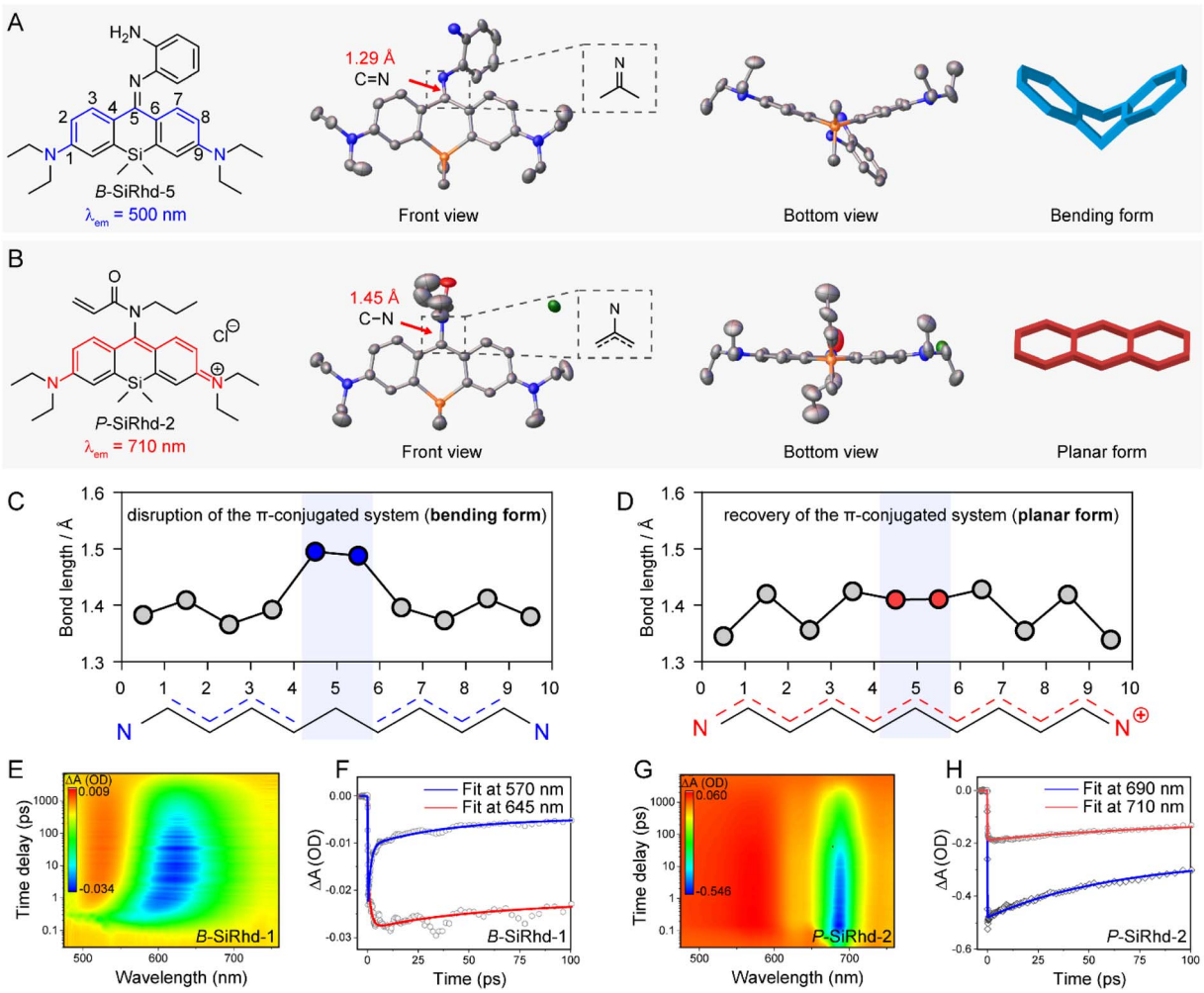

Fig. 3 Revealing the molecular bent-to-planar configuration change between imino and amino forms resulting in a significant wavelength shift. Chemical structures and single-crystal X-ray structures of (A) B-SiRhd-5 and (B) P-SiRhd-2. Note: solvent molecules and H atoms are omitted for clarity. Bond lengths of the carbon–carbon and carbon–nitrogen bonds of B-SiRhd-5 (C, bent-form) and P-SiRhd-2 (D, planar-form) along the conjugated path according to the crystal structure. (E) Femtosecond time-resolved transient absorption (TA) spectroscopy (contour plot) of B-SiRhd-1 in CH_3CN. (F) A comparison of the B-SiRhd-1 TA kinetic traces at 645 and 570 nm (λ_{ex} = 460 nm). (G) TA spectroscopy (contour plot) of P-SiRhd-2 in CH_3CN. (H) A comparison of the P-SiRhd-2 TA kinetic traces at 710 and 690 nm (λ_{ex} = 680 nm).

skeletal conformation could expand the π-conjugation,[38,39] it is believed that tailoring the nature of the *meso*-position substituent in the conjugated system would play a key role in the development of NIR Si-rhodamine scaffolds.

According to single-crystal analysis, distinctly different π-delocalization was observed from *meso*-nitrogen substituted Si-rhodamines due to the electron density perturbation, and therefore the configuration in the molecular solution-state should be further investigated. With this in mind, we subsequently carried out femtosecond time-resolved transient absorption (TA) spectroscopy experiments. As shown in Fig. 3E, the time-resolved experiments of B-SiRhd-1 showed a red shift stimulated emission band, which is in agreement with the flexible molecular geometry (*i.e.*, bent configuration) of B-SiRhd-5 from the single-crystal analysis. More importantly, the transient absorption of B-SiRhd-1 kinetic traces at 570 nm and 645 nm clearly denotes an internal conversion in the excited state[40–42] (Fig. 3F and S11†), further confirming that the B-SiRhd scaffold is flexibly bent in the molecular solution state. In contrast, P-SiRhd-2 displayed a still stimulated emission band over time (Fig. 3G and H), which implies that the Si-rhodamine scaffold is rigid in both the crystalline solid-state and solution-state (*i.e.*, planar configuration). All these results further confirm that the regulation of the *meso*-nitrogen substituent in the Cl-SiRhd scaffold can switch intramolecular π-electron delocalization, thereby resulting in flipping between the disruption and recovery of the polymethine π-electron system.

Constructing ratiometric NIR probes with minimized spectral crosstalk

The above experiments demonstrated that the alteration of π-electron delocalization in Si-rhodamines could generate a crosstalk-free dual-channel response. We thus hypothesized that high-performance ratiometric fluorescent probes[43–48] could be designed *via* switching Si-rhodamines between the bent and planar configurations (Fig. 4A). Consequently, the following functionalized B-SiRhd/P-SiRhd probes were designed: B-SiRhd-3 with a 1-(2-aminoethyl)-3-phenylthiourea group for sensing Hg^{2+}, B-SiRhd-4 with a 4-aminobutyric acid group for sensing phosgene and P-SiRhd-1 with the allyl propylcarbamate group for sensing Pd(0). As shown in Fig. 4B–J and S12–S15,† the crosstalk-free ratiometric responses were observed in all test assays.

For example, upon the addition of Hg^{2+}, B-SiRhd-3 exhibited a remarkable shift in the absorption spectra, along with an obvious color change from yellow to green. Specifically, the absorption peak at 488 nm sharply decreased, and an increasing band centered at 690 nm was simultaneously observed, along with a distinct isosbestic point at around 550 nm (Fig. 4C). Concomitantly, when excited at an isosbestic point of 550 nm, an obvious decrease in the emission spectra at 610 nm and a sharp increase at 710 nm were also observed in the emission spectra (Fig. 4D, S16 and S17†). Importantly, this crosstalk-free ratiometric response not only contributes to the accurate measurement of dual-channel emission intensity, but also results in a huge ratiometric value (Fig. S18†). To our delight, similar emission profiles and crosstalk-free responses were also observed in B-SiRhd-3 and P-SiRhd-1 towards phosgene and Pd(0), respectively (Fig. S19 and S20†). Furthermore, the crosstalk-free ratiometric bioimaging in cells and zebrafish demonstrated that B-SiRhd-3 can real-time track the uptake of Hg^{2+} in living cells and zebrafish (Fig. 4K, L and S21†). All these above results showed that the bent/planar switchable Si-rhodamines enable crosstalk-free ratiometric analysis and serve as a generalizable platform for detecting various chemical species.

Enabling simultaneously activatable NIR-II, photoacoustic, and photothermal signals

It remains quite challenging to rationally regulate absorption and emission in the NIR-II region, and these bottlenecks severely hinder the applicability of such probes for *in vivo* biosensing.[49–54] Given that the asymmetric bent form (B-SiRhd with NIR-I emission) could be transformed to planar-form Si-rhodamines (P-SiRhd with NIR-II emission) (Fig. 2F and 5A), rational modulation of the NIR-II emission could be achieved *via* bent-to-planar configuration change. In this regard, various NIR-II fluorescent probes could be constructed *via* using our B-SiRhd/P-SiRhd chromophores.

The asymmetric Si-rhodamine probes B-SiRhd-6 and B-SiRhd-7 were obtained by using a 1-(2-aminoethyl)-3-phenylthiourea moiety as the Hg^{2+} responsive site, and an *o*-phenylenediamine moiety as the nitric oxide (NO) responsive site, respectively. To our delight, both B-SiRhd-6 (Fig. S22–S26†) and B-SiRhd-7 displayed remarkable lighting-up NIR-II fluorescence in response to their respective target analytes. For example, B-SiRhd-7 initially displayed two main absorptions at 420 and 580 nm with an emission peak at 520 nm. The detection of NO resulted in a new sharply increased NIR-I absorption band centered at 800 nm (Fig. 5B), accompanied by a reduction of the original absorption bands with a limit of detection of 0.3 μM (Fig. S27†). Concomitantly, a new significantly increased emission band in the NIR-II region around 1050 nm ($\lambda_{ex} = 800$ nm) was observed, along with the decrease of the 520 nm emission (Fig. 5C, D and S28–S33†). Such an obvious NIR-II fluorescence enhancement (20-fold) is attributed to the NO-induced bent-to-planar transformation of Si-rhodamine (Fig. 5A). We summarize these photophysical properties of Cl-SiRhd-based fluorophores (Table S1†). Impressively, P-SiRhd-7 exhibits excellent photostability compared to the traditional NIR-II fluorophore, which is a critical property in *in vivo* fluorescence imaging (Fig. S34†). All these results demonstrated that our bent-to-planar strategy enables not only the construction of dual-channel crosstalk-free ratiometric probes, but also the construction of turn-on probes with NIR-II fluorescence.

Inspired by the NO-induced sharp enhancement of the absorption at 800 nm, we reasoned that B-SiRhd-7 could be a promising chromophore for activatable photothermal (PT) therapy and photoacoustic (PA) imaging.[55–60] As shown in Fig. 5E, upon treatment with NO, the probe B-SiRhd-7 exhibited a clear NIR-photothermal effect upon exposure to 808 nm NIR

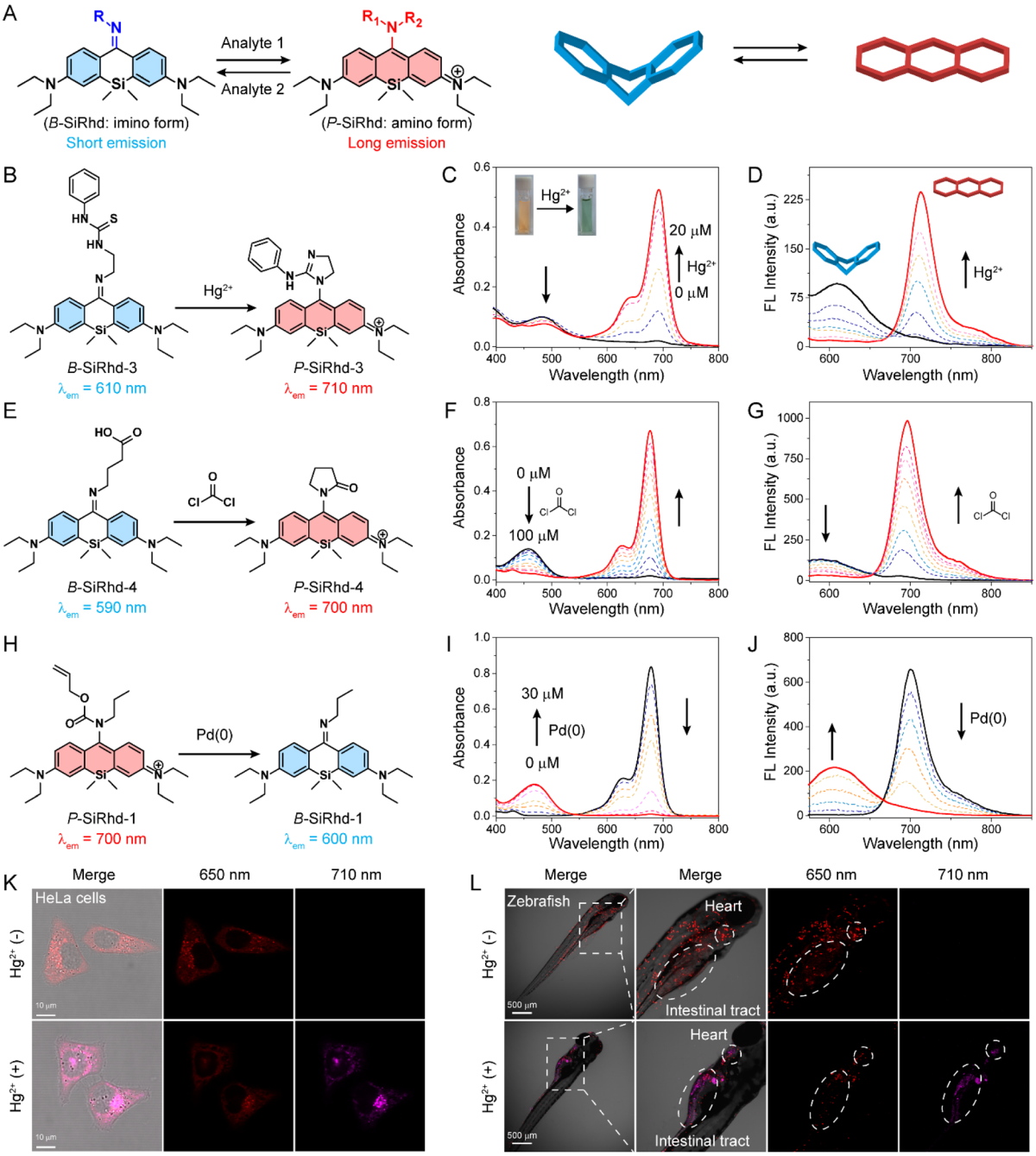

Fig. 4 A generalizable method for ratiometric NIR sensing with minimized crosstalk. (A) Using the designed bent/planar switchable fluorophores, we are able to construct NIR ratiometric probes. Chemical structures of bent/planar switchable probes with different biomolecular-recognition groups towards Hg^{2+} (B), phosgene (E), and Pd(0) (H). Absorption (C, F and I) and fluorescence (D, G and J) spectra of B-SiRhd-3, B-SiRhd-4, and P-SiRhd-1 for various analytes (λ_{ex} = 550 nm). (K and L) Dual-channel fluorescence imaging of Hg^{2+} with minimized crosstalk in cells and zebrafish (incubated with B-SiRhd-3, without and with Hg^{2+}).

light laser irradiation. The repeatable temperature increases (even after five cycles of heating and cooling) indicated that this NO-activatable probe B-SiRhd-7 has excellent photo-thermal stability as a potential PTT agent (Fig. 5F and S35–S37†). Furthermore, we also explored the NO-induced PA signal from the response of B-SiRhd-7. Notably, the corresponding opto-acoustic signal at approximately 800 nm is enhanced for the detection of NO with good linear quantifiability (Fig. 5G) and high selectivity (Fig. 5H and S38†). Taken together, all these spectral results including single-crystals and time-resolved transient absorption analysis clearly demonstrated that the B-SiRhd/P-SiRhd platform could serve as a generalizable method for engineering activatable NIR-II probes with PT and PA signals.

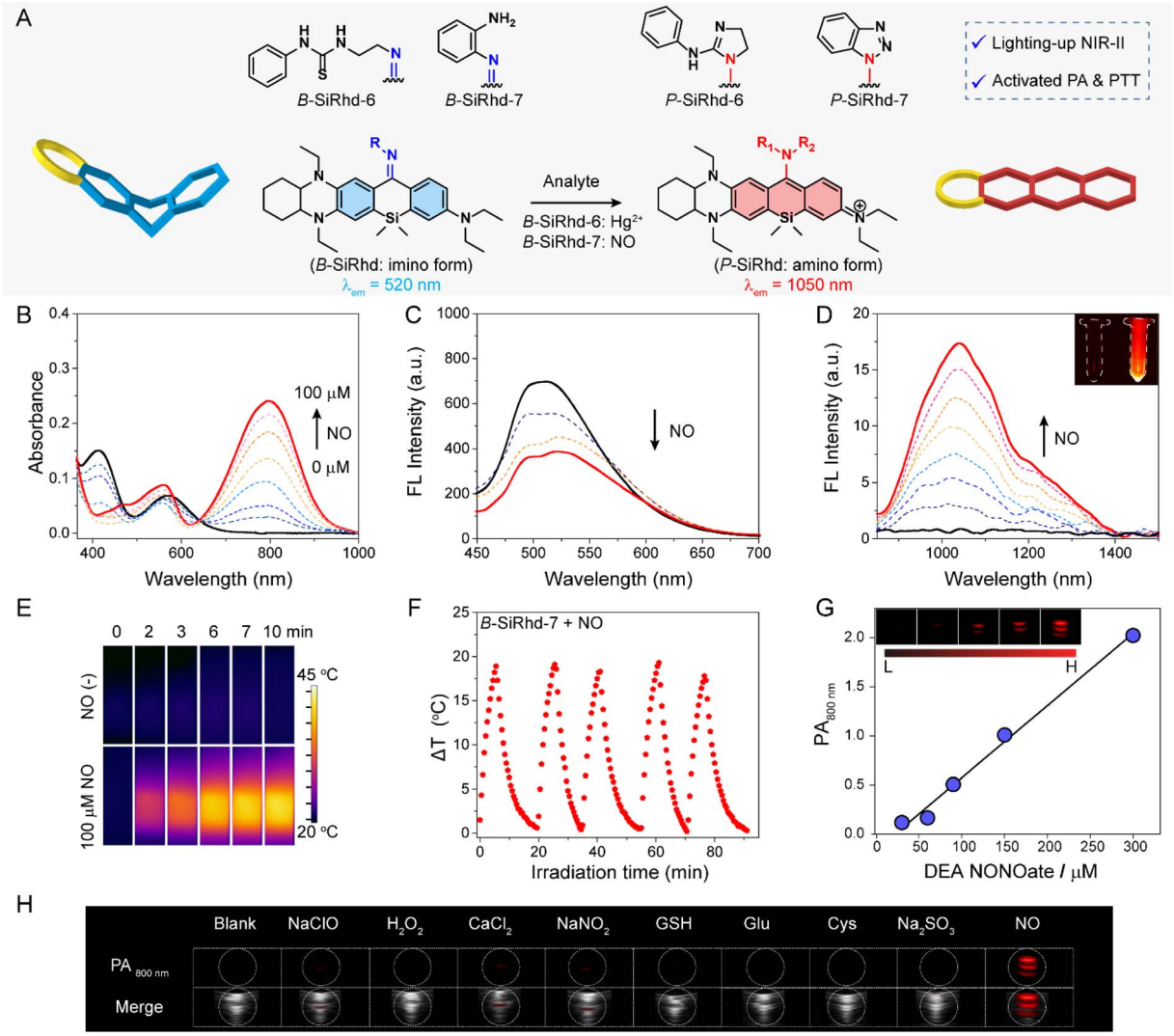

Fig. 5 The molecular bent-to-planar strategy for lighting-up NIR-II sensing. (A) Schematic illustration of the sensing mechanism for B-SiRhd-6 and B-SiRhd-7 towards Hg^{2+} and NO, respectively. Activatable NIR-II response: absorption (B) and fluorescence emission (C and D) spectra of B-SiRhd-7 (10 μM) in the presence of NO in a mixed solution. (E) Photothermal activation: thermal infrared image of B-SiRhd-7 (20 μM) in the presence of NO under 808 nm laser irradiation (2 W cm^{-2}). (F) Excellent photothermal stability: the variation of temperatures during five cycles of heating–cooling processes under 808 nm laser irradiation of B-SiRhd-7 (20 μM) with 100 μM NO. (G) Photoacoustic (PA) activation: plot of PA_{800nm} of B-SiRhd-7 against the concentration of NO. (H) *In vitro* PA images of the solution of B-SiRhd-7 in the presence of various biologically relevant species at 800 nm.

Lighting-up NIR-II fluorescence for real-time *in situ* tracking inflammation in the liver, intestine and AD mice brain

The diagnosis of chronic diseases is of great significance for the timely implementation of medical intervention. Chronic inflammation plays a key role in the development and progression of many chronic diseases, such as inflammatory bowel disease (IBD) and Alzheimer's disease (AD), and can lead to increases in morbidity.[61,62] Therefore, accurate mapping of inflammation will provide critical information to better understand its role in the onset and progression of chronic diseases. Activatable NIR-II imaging is a powerful approach to interrogate intact living samples in real time with spatial resolution due to its deep penetration and high-fidelity imaging capabilities. It has been widely applied for non-invasive real-time sensing and disease diagnosis in living systems.

Our new method of analyte-controlled molecular configuration changes for lighting-up NIR-II detection fits in well with disease diagnosis in living systems. Herein, to validate our strategy of expanding light-up NIR-II sensors with the real-time *in vivo* imaging capability, we chose the construction of an inflammation sensing system based on effective interaction of inflammatory factors for *in situ* generation of NO in deep tissue. We next assessed the capability of B-SiRhd-7 for *in vivo* monitoring endogenous NO levels in LPS-induced inflammation and Alzheimer's disease mice (Fig. 6). Because NO is a lipid-permeable free radical molecule, liposomal nanoparticles would be better employed to encapsulate B-SiRhd-7 for tracking NO fluctuation. With this in mind, stable lipid-based supramolecular nanoparticles were fabricated by self-assembly of colipids (phosphatidylcholine, DSPE-PEG-

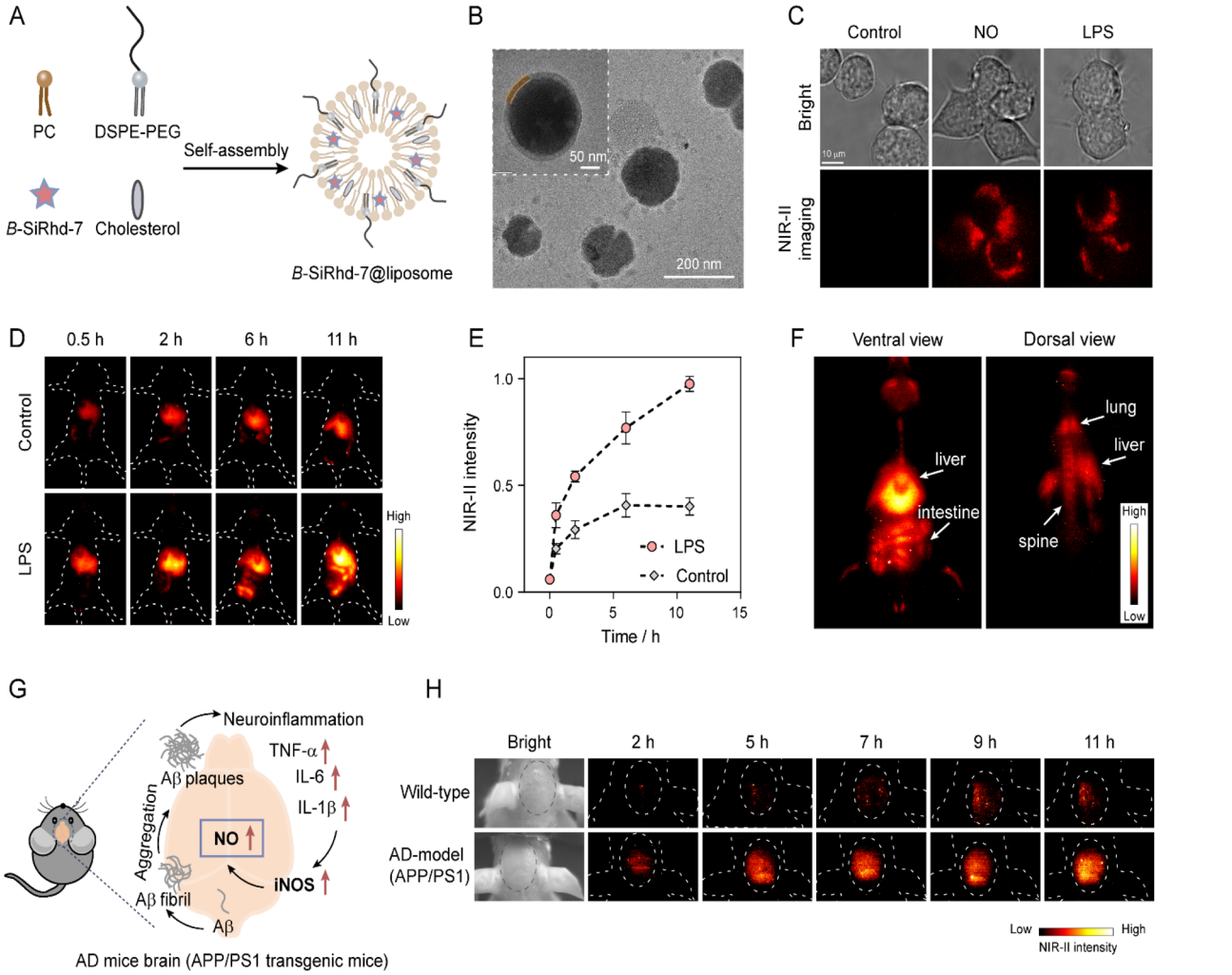

Fig. 6 *In vivo* NIR-II imaging of nitric oxide in LPS-induced inflammation and Alzheimer disease (AD) mice. (A) Schematics showing the synthesis of B-SiRhd-7@liposome. Cholesterol and NO probe B-SiRhd-7 were loaded into a stable liposomal system facilitated by the self-assembly of colipids (DSPE-PEG and phosphatidyl choline (PC)). (B) TEM image showing a B-SiRhd-7@liposome. (C) NIR-II fluorescence imaging of NO in RAW264.7 cells (incubated with B-SiRhd-7@liposome, without and with exogenous or endogenous NO). Notes: λ_{ex} = 808 nm, and 900 nm emission filter. (D) Representative images of mice receiving intravenously B-SiRhd-7@liposome (0.4 mM, 200 μL) pretreated with LPS or saline (control) intraperitoneally at a different time point. (E) The normalized fluorescence intensity over time in Fig. 6D. The maximum fluorescence intensity (11 h) is defined as 1.0. Data are presented as mean ± SD (n = 3). (F) Biodistribution of B-SiRhd-7@liposome in the LPS-induced mouse in the ventral view (26 h) and dorsal view (28 h) after tail-vein injection of B-SiRhd-7@liposome. (G) Purposed biological synthesis route of NO in AD mouse brains. (H) *In vivo* fluorescence imaging of NO in wild-type and AD-model (APP/PS1) mice brains for 11 h *via* intravenous injection of 200 μL of 0.4 mM B-SiRhd-7@liposomes. λ_{ex} = 808 nm, and 1100 nm long-pass filter.

2000, and cholesterol) facilitated by hydrophilic and hydrophobic interactions. Indeed, hydrophobic B-SiRhd-7 occupies the spaces between the lipid bilayer constituting the B-SiRhd-7@liposome system[63] (Fig. 6A). The hydrodynamic diameter was evaluated using dynamic light scattering and was found to be *ca.* 125 nm (Fig. S39 and S40†). Transmission electron microscopy revealed the nanoparticles to have a clear structure of the lipid bilayer (Fig. 6B). Taking the above results together, we successfully prepared spherical core–shell structured liposome nanoparticles with a homogeneous particle size.

Firstly, we evaluated the NIR-II fluorescence response ability of B-SiRhd-7@liposome towards NO in living cells, and a RAW 264.7 cell was chosen as a model cell line. As shown in Fig. 6C and S41,† when RAW264.7 cells were preloaded with B-SiRhd-7@liposome (10 μM) for 30 min, dim fluorescence was detected in cells. However, after the cells were incubated with NO (10 μM) for another 10 min, a distinct enchantment of NIR-II fluorescence (λ_{ex} = 808 nm and 900 nm emission filter) of the cells was observed. Similarly, remarkable NIR-II fluorescence was found in the lipopolysaccharide (LPS, 1 μg mL^{-1}) pretreatment group, in which LPS could induce an inflammatory response in cells to produce NO. Cellular test results indicated that B-SiRhd-7@liposome enables real-time tracking of the alteration of endogenous NO levels.

Encouraged by *in vivo* cellular imaging results, we further examined B-SiRhd-7@liposome for monitoring the fluctuation

of NO levels in LPS-induced inflammation mice models. Mice were treated with either LPS (1 mg mL^{-1}, 4 mg kg^{-1}) or saline (as a control group) intraperitoneally. After 6 h, B-SiRhd-7@liposome (0.4 mM, 200 μL) was intravenously injected into the tail of mice. The images were collected upon light irradiation at 808 nm, with a 1100 nm long-pass filter. The LPS pretreated group displayed a faster liver response and clearer intestinal imaging than that of the control group (Fig. 6D, E and S42†). These results showed that B-SiRhd-7@liposome has the capability of effectively real-time monitoring of multi-organ inflammation induced by intraperitoneal LPS injection[64,65] rather than just a single liver injury. Indeed, the real-time biodistribution from the probe provides important evidence to assess their biosafety for further clinical applications. Particularly, the light-up NIR-II fluorescence with deep tissue penetration makes it possible to directly visualize B-SiRhd-7@liposome's biodistribution. As illustrated in Fig. 6F, after the administration of the probe into LPS-induced inflammation models, B-SiRhd-7@liposomes are distributed especially in the mononuclear phagocyte system (MPS)-enriched organs, such as liver, intestine, lung and spine (Fig. S43–S45†). All these *in vivo* imaging results indicated that the light-up NIR-II fluorescence signals of B-SiRhd-7@liposomes can be used as a powerful tool for real-time *in situ* monitoring of multi-organ inflammation, especially in intestinal inflammation.

We further evaluated the biosensing efficacy of lighting-up NIR-II B-SiRhd-7@liposome in the Alzheimer's disease brain. Neuroinflammation has demonstrated an important role in the pathogenesis of Alzheimer's disease (AD), which is the most prevalent form of dementia.[66–68] Previous work has proven that the expression of the inducible nitric oxide synthase (iNOS) level in the APP/PS1 mice brain was much higher than that of wild-type (WT) mice, thereby leading to the overproduction of NO (Fig. 6G).[66] We envision that B-SiRhd-7@liposome is suitable for *in vivo* monitoring the fluctuation of NO in the AD brains. To confirm this feasibility, 12 month-old male AD-model (APP/PS1 transgenic) mice and age-matched wild-type WD mice were chosen to study the brain kinetics by intravenous injection of B-SiRhd-7@liposome. As shown in Fig. 6H, nearly all of the NIR-II fluorescence signals were centralized in the brain compartments and could be efficiently captured. In particular, the fluorescence intensity of B-SiRhd-7@liposome in the brain regions of the APP/PS1 mice was higher than that in the control of wild-type mice at 11 h post injection, indicative of specifically trapping NO *in vivo* with probe B-SiRhd-7@liposome (Fig. S46†). These directly *in situ* brain results evidenced that the overexpression of NO is one of the hallmarks of AD mice. The above *in vivo* imaging results illustrated that our bent-to-planar conformational design strategy for NIR-II Si-rhodamine probes makes a breakthrough in directly *in situ* mapping inflammation (neuroinflammation and LPS-induced inflammation).

Conclusions

Harnessing a concise molecular configuration-tunable strategy, *i.e.*, bent-to-planar transformation in Si-rhodamines, we have successfully developed NIR-II Si-rhodamines with a large Stokes shift (*ca.* 250 nm) for directly *in situ* mapping inflammatory (neuroinflammation and LPS-induced inflammation). This breakthrough establishes an innovative rehybridization of NIR-I&II fluorogenic framework Cl-SiRhd and thus activates configuration change to greatly expand the Si-rhodamine spectral window. With single-crystals and transient absorption experiments, we confirmed that the imino form of *meso*-nitrogen with sp^2 hybridization results in a bent configuration, which disrupts π-electron delocalization and accounts for a short emission wavelength. In contrast, when *meso*-nitrogen undergoes sp^3 hybridization, the amino form leads to a planar conformation, which recovers the π-conjugation and lights up NIR I&II emissions. These unique NIR-II lighting-up Si-rhodamine probes (B-SiRhd-6 and B-SiRhd-7) with crosstalk-free responses successfully perform *in vivo* tracking of LPS-induced multi-organ inflammation, including intestinal inflammation in deep physiological anatomical locations. Notably, for the first time, B-SiRhd-7@liposomes with light-up NIR-II fluorescence signals makes a breakthrough in monitoring abnormal nitric oxide levels in the Alzheimer's brain. We anticipate that this *de novo* conformation-dependent strategy of Si-rhodamine probes paves a new way for expanding NIR-II bio-analytical toolboxes in both basic life science research and clinical applications.

Data availability

Additional experimental details and data are provided in the ESI.† The accession numbers for the crystallographic data reported in this paper are CCDC: 2119838, 2119842 and 2132279. All procedures involving animals were conducted in accordance with the National Research Council Guide for Care and Use of Laboratory Animals. APP/PS1 transgenic mice (Jiangsu Huachuang Sino Pharmatech Co., Ltd; approval number: SCXK (Jiangsu) 2020-0009) or BALB/cA nude mice (Shanghai SLAC Laboratory Animal Co. Ltd; approval number: SCXK (Shanghai) 2022-0004) were used for animal experiments.

Author contributions

All the experiments were conducted by Q. X., Y. Z., M. Z., C. Y., and W. M. with the supervision of W. Z. and Z. G. All authors discussed the results and co-wrote the manuscript.

Conflicts of interest

The authors declare no competing financial interest.

Acknowledgements

This work was supported by NSFC/China (22225805 and 32121005), National Key Research and Development Program of China (2021YFA0910000), Shanghai Municipal Science and Technology Major Project (Grant 2018SHZDZX03, 21JC1401700), Innovation Program of Shanghai Municipal Education Commission, Shanghai Frontier Science Research Base of Optogenetic Techniques for Cell Metabolism (Shanghai

Municipal Education Commission, grant 2021 Sci & Tech 03-28), and Programme of Introducing Talents of Discipline to Universities (B16017), and sponsored by Shanghai Pujiang Program (21PJD038). We thank Weimin Liu, ShanghaiTech University, for the femtosecond time-resolved transient absorption spectroscopy experimental support.

Notes and references

1 T. C. Pham, V. N. Nguyen, Y. Choi, S. Lee and J. Yoon, *Chem. Rev.*, 2021, **121**, 13454–13619.
2 Q. Yao, J. Fan, S. Long, X. Zhao, H. Li, J. Du, K. Shao and X. Peng, *Chem*, 2022, **8**, 197–209.
3 X. Wu, H. Li, E. Lee and J. Yoon, *Chem*, 2020, **6**, 2893–2901.
4 C. Li, G. Chen, Y. Zhang, F. Wu and Q. Wang, *J. Am. Chem. Soc.*, 2020, **142**, 14789–14804.
5 E. M. Surender, S. J. Bradberry, S. A. Bright, C. P. McCoy, D. C. Williams and T. Gunnlaugsson, *J. Am. Chem. Soc.*, 2017, **139**, 381–388.
6 J.-T. Hou, K.-K. Yu, K. Sunwoo, W. Y. Kim, S. Koo, J. Wang, W. X. Ren, S. Wang, X.-Q. Yu and J. S. Kim, *Chem*, 2020, **6**, 832–866.
7 C. Li, Y. Xu, L. Tu, M. Choi, Y. Fan, X. Chen, J. L. Sessler, J. S. Kim and Y. Sun, *Chem. Sci.*, 2022, **13**, 6541–6549.
8 T. Wang, S. Wang, Z. Liu, Z. He, P. Yu, M. Zhao, H. Zhang, L. Lu, Z. Wang, Z. Wang, W. Zhang, Y. Fan, C. Sun, D. Zhao, W. Liu, J. G. Bunzli and F. Zhang, *Nat. Mater.*, 2021, **20**, 1571–1578.
9 L. Wu, J. Liu, P. Li, B. Tang and T. D. James, *Chem. Soc. Rev.*, 2021, **50**, 702–734.
10 A. L. Antaris, H. Chen, K. Cheng, Y. Sun, G. Hong, C. Qu, S. Diao, Z. Deng, X. Hu, B. Zhang, X. Zhang, O. K. Yaghi, Z. R. Alamparambil, X. Hong, Z. Cheng and H. Dai, *Nat. Mater.*, 2016, **15**, 235–242.
11 C. Li, Y. Xu, L. Tu, M. Choi, Y. Fan, X. Chen, J. L. Sessler, J. S. Kim and Y. Sun, *Chem. Sci.*, 2022, **13**, 6541–6549.
12 E. D. Cosco, J. R. Caram, O. T. Bruns, D. Franke, R. A. Day, E. P. Farr, M. G. Bawendi and E. M. Sletten, *Angew. Chem., Int. Ed.*, 2017, **56**, 13126–13129.
13 E. D. Cosco, A. L. Spearman, S. Ramakrishnan, J. G. P. Lingg, M. Saccomano, M. Pengshung, B. A. Arus, K. C. Y. Wong, S. Glasl, V. Ntziachristos, M. Warmer, R. R. McLaughlin, O. T. Bruns and E. M. Sletten, *Nat. Chem.*, 2020, **12**, 1123–1130.
14 Y. Fang, J. Shang, D. Liu, W. Shi, X. Li and H. Ma, *J. Am. Chem. Soc.*, 2020, **142**, 15271–15275.
15 Z. Lei and F. Zhang, *Angew. Chem., Int. Ed.*, 2021, **60**, 16294–16308.
16 T. B. Ren, Z. Y. Wang, Z. Xiang, P. Lu, H. H. Lai, L. Yuan, X. B. Zhang and W. Tan, *Angew. Chem., Int. Ed.*, 2021, **60**, 800–805.
17 J. Li, Y. Dong, R. Wei, G. Jiang, C. Yao, M. Lv, Y. Wu, S. H. Gardner, F. Zhang, M. Y. Lucero, J. Huang, H. Chen, G. Ge, J. Chan, J. Chen, H. Sun, X. Luo, X. Qian and Y. Yang, *J. Am. Chem. Soc.*, 2022, **144**, 14351–14362.
18 L. Wang, M. Tran, E. D'Este, J. Roberti, B. Koch, L. Xue and K. Johnsson, *Nat. Chem.*, 2020, **12**, 165–172.
19 S. Takahashi, Y. Kagami, K. Hanaoka, T. Terai, T. Komatsu, T. Ueno, M. Uchiyama, I. Koyama-Honda, N. Mizushima, T. Taguchi, H. Arai, T. Nagano and Y. Urano, *J. Am. Chem. Soc.*, 2018, **140**, 5925–5933.
20 L. Wang, W. Du, Z. Hu, K. Uvdal, L. Li and W. Huang, *Angew. Chem., Int. Ed.*, 2019, **58**, 14026–14043.
21 M. Fu, Y. Xiao, X. Qian, D. Zhao and Y. Xu, *Chem. Commun.*, 2008, **15**, 1780–1782.
22 N. Lardon, L. Wang, A. Tschanz, P. Hoess, M. Tran, E. D'Este, J. Ries and K. Johnsson, *J. Am. Chem. Soc.*, 2021, **143**, 14592–14600.
23 A. N. Butkevich, G. Lukinavicius, E. D'Este and S. W. Hell, *J. Am. Chem. Soc.*, 2017, **139**, 12378–12381.
24 J. B. Grimm, A. N. Tkachuk, L. Xie, H. Choi, B. Mohar, N. Falco, K. Schaefer, R. Patel, Q. Zheng, Z. Liu, J. Lippincott-Schwartz, T. A. Brown and L. D. Lavis, *Nat. Methods*, 2020, **17**, 815–821.
25 Y. Koide, Y. Urano, K. Hanaoka, W. Piao, M. Kusakabe, N. Saito, T. Terai, T. Okabe and T. Nagano, *J. Am. Chem. Soc.*, 2012, **134**, 5029–5031.
26 T. B. Ren, W. Xu, W. Zhang, X. X. Zhang, Z. Y. Wang, Z. Xiang, L. Yuan and X. B. Zhang, *J. Am. Chem. Soc.*, 2018, **140**, 7716–7722.
27 C. Yan, Z. Guo, Y. Liu, P. Shi, H. Tian and W. H. Zhu, *Chem. Sci.*, 2018, **9**, 6176–6182.
28 P. Horvath, P. Sebej, T. Solomek and P. Klan, *J. Org. Chem.*, 2015, **80**, 1299–1311.
29 K. H. Kim, S. Singha, Y. W. Jun, Y. J. Reo, H. R. Kim, H. G. Ryu, S. Bhunia and K. H. Ahn, *Chem. Sci.*, 2019, **10**, 9028–9037.
30 L. Wu and K. Burgess, *Org. Lett.*, 2008, **10**, 1779–1782.
31 H. Zhang, J. Liu, L. Wang, M. Sun, X. Yan, J. Wang, J. P. Guo and W. Guo, *Biomaterials*, 2018, **158**, 10–22.
32 Z. Guo, S. Park, J. Yoon and I. Shin, *Chem. Soc. Rev.*, 2014, **43**, 16–29.
33 X. Peng, F. Song, E. Lu, Y. Wang, W. Zhou, J. Fan and Y. Gao, *J. Am. Chem. Soc.*, 2005, **127**, 4170–4171.
34 Y. Zhang, S. Xia, M. Fang, W. Mazi, Y. Zeng, T. Johnston, A. Pap, R. L. Luck and H. Liu, *Chem. Commun.*, 2018, **54**, 7625–7628.
35 Y. Q. Sun, J. Liu, H. Zhang, Y. Huo, X. Lv, Y. Shi and W. Guo, *J. Am. Chem. Soc.*, 2014, **136**, 12520–12523.
36 M. S. Frei, P. Hoess, M. Lampe, B. Nijmeijer, M. Kueblbeck, J. Ellenberg, H. Wadepohl, J. Ries, S. Pitsch, L. Reymond and K. Johnsson, *Nat. Commun.*, 2019, **10**, 4580.
37 T. Pastierik, P. Sebej, J. Medalova, P. Stacko and P. Klan, *J. Org. Chem.*, 2014, **79**, 3374–3382.
38 Z. Zhang, Y. S. Wu, K. C. Tang, C. L. Chen, J. W. Ho, J. Su, H. Tian and P. T. Chou, *J. Am. Chem. Soc.*, 2015, **137**, 8509–8520.
39 Z. Zhang, C. L. Chen, Y. A. Chen, Y. C. Wei, J. Su, H. Tian and P. T. Chou, *Angew. Chem., Int. Ed.*, 2018, **57**, 9880–9884.
40 W. Chi, Q. Qiao, R. Lee, W. Liu, Y. S. Teo, D. Gu, M. J. Lang, Y. T. Chang, Z. Xu and X. Liu, *Angew. Chem., Int. Ed.*, 2019, **58**, 7073–7077.
41 L. Shi, C. Yan, Z. Guo, W. Chi, J. Wei, W. Liu, X. Liu, H. Tian and W. H. Zhu, *Nat. Commun.*, 2020, **11**, 793.

42 C. Wang, W. Chi, Q. Qiao, D. Tan, Z. Xu and X. Liu, *Chem. Soc. Rev.*, 2021, **50**, 12656–12678.
43 Q. Lan, P. Yu, K. Yan, X. Li, F. Zhang and Z. Lei, *J. Am. Chem. Soc.*, 2022, **144**, 21010–21015.
44 K. Xin, X. Li, Y. Guo, Y. Zhong, J. Wang, H. Yang, J. Zhao, C. Guo, Y. Huang, Z. Lei, Y.-L. Ying, X. Luo, H. Wang, X. Qian, W. Yang, X. Liang and Y. Yang, *CCS Chem.*, 2021, **3**, 2307–2315.
45 X. Zhang, Y. Xiao and X. Qian, *Angew. Chem., Int. Ed.*, 2008, **47**, 8025–8029.
46 X. Zhou, L. Lesiak, R. Lai, J. R. Beck, J. Zhao, C. G. Elowsky, H. Li and C. I. Stains, *Angew. Chem., Int. Ed.*, 2017, **56**, 4197–4200.
47 T. Zhou, Q. Wang, M. Liu, Z. Liu, Z. Zhu, X. Zhao and W. H. Zhu, *Aggregate*, 2021, **2**, e22.
48 J. H. Kim, P. Verwilst, M. Won, J. Lee, J. L. Sessler, J. Han and J. S. Kim, *J. Am. Chem. Soc.*, 2021, **143**, 14115–14124.
49 W. Wang, Q. Yang, Y. Du, X. Zhou, X. Du, Q. Wu, L. Lin, Y. Song, F. Li, C. Yang and W. Tan, *Angew. Chem., Int. Ed.*, 2020, **59**, 2628–2633.
50 D. Liu, Z. He, Y. Zhao, Y. Yang, W. Shi, X. Li and H. Ma, *J. Am. Chem. Soc.*, 2021, **143**, 17136–17143.
51 H. Lin, S. Gao, C. Dai, Y. Chen and J. Shi, *J. Am. Chem. Soc.*, 2017, **139**, 16235–16247.
52 G. S. Hong, A. L. Antaris and H. J. Dai, *Nat. Biomed. Eng.*, 2017, **1**, 0010.
53 C. S. L. Rathnamalala, J. N. Gayton, A. L. Dorris, S. A. Autry, W. Meador, N. I. Hammer, J. H. Delcamp and C. N. Scott, *J. Org. Chem.*, 2019, **84**, 13186–13193.
54 Y. Shi, W. Yuan, Q. Liu, M. Kong, Z. Li, W. Feng, K. Hu and F. Li, *ACS Mater. Lett.*, 2019, **1**, 418–424.
55 J. Qi, J. Li, R. Liu, Q. Li, H. Zhang, J. W. Y. Lam, R. T. K. Kwok, D. Liu, D. Ding and B. Z. Tang, *Chem*, 2019, **5**, 2657–2677.
56 M. Shi, Z. Fu, W. Pan, Y. Chen, K. Wang, P. Zhou, N. Li and B. Tang, *Angew. Chem., Int. Ed.*, 2021, **60**, 13564–13568.
57 H. Gao, X. Duan, D. Jiao, Y. Zeng, X. Zheng, J. Zhang, H. Ou, J. Qi and D. Ding, *Angew. Chem., Int. Ed.*, 2021, **60**, 21047–21055.
58 Y. Wu, S. Huang, J. Wang, L. Sun, F. Zeng and S. Wu, *Nat. Commun.*, 2018, **9**, 3983.
59 X. Li, J. F. Lovell, J. Yoon and X. Chen, *Nat. Rev. Clin. Oncol.*, 2020, **17**, 657–674.
60 Y. Y. Zhao, L. Zhang, Z. Chen, B. Y. Zheng, M. Ke, X. Li and J. D. Huang, *J. Am. Chem. Soc.*, 2021, **143**, 13980–13989.
61 C. J. Reinhardt, E. Y. Zhou, M. D. Jorgensen, G. Partipilo and J. Chan, *J. Am. Chem. Soc.*, 2018, **140**, 1011–1018.
62 Z. He, D. Liu, Y. Liu, X. Li, W. Shi and H. Ma, *Anal. Chem.*, 2022, **94**, 10256–10262.
63 A. Ramesh, S. Kumar, A. Brouillard, D. Nandi and A. Kulkarni, *Adv. Mater.*, 2020, **32**, e2000648.
64 M. Nighot, R. Al-Sadi, S. Guo, M. Rawat, P. Nighot, M. D. Watterson and T. Y. Ma, *Am. J. Pathol.*, 2017, **187**, 2698–2710.
65 G. Kolios, V. Valatas and S. G. Ward, *Immunology*, 2004, **113**, 427–437.
66 P. Wang, L. Yu, J. Gong, J. Xiong, S. Zi, H. Xie, F. Zhang, Z. Mao, Z. Liu and J. S. Kim, *Angew. Chem., Int. Ed.*, 2022, **61**, e202206894.
67 F. Leng and P. Edison, *Nat. Rev. Neurol.*, 2021, **17**, 157–172.
68 A. Guerrero, B. De Strooper and I. L. Arancibia-Carcamo, *Trends Neurosci.*, 2021, **44**, 714–727.